Research Square

Preprints are preliminary reports that have not undergone peer review.
They should not be considered conclusive, used to inform clinical practice,
or referenced by the media as validated information.

# Intelligent Ultrasonic Characterization of Bonding Conditions in Aircraft Honeycomb Sandwich Composite Panels

**Yating Ni**
Nanchang Hangkong University
**Zhenhua Chen**
zhenhuachen@yeah.net
Nanchang Hangkong University
**Simin Tu**
Jiangxi Hongdu Aviation Industry Group Co., Ltd.
**Junyan Zhang**
Jiangxi Hongdu Aviation Industry Group Co., Ltd.
**Liu Yang**
Jiangxi Hongdu Aviation Industry Group Co., Ltd.
**Chao Lu**
Nanchang Hangkong University

**Research Article**

**Keywords:** Honeycomb sandwich composite panel, Water-jet-coupled focused ultrasonic testing, Deep learning, Intelligent classification, Bonding condition, Ultrasonic C-scan image

**Posted Date:** November 4th, 2026

**DOI:** https://doi.org/10.21203/rs.3.rs-10659977/v1

**License:** This work is licensed under a Creative Commons Attribution 4.0 International License.
Read Full License

**Additional Declarations:** No competing interests reported.

# Intelligent Ultrasonic Characterization of Bonding Conditions in Aircraft Honeycomb Sandwich Composite Panels

Yating Ni[1], Zhenhua Chen[1]*, Simin Tu[2], Junyan Zhang[2], Liu Yang[2], Chao Lu[1]

[1] Key Laboratory of Nondestructive Testing, Ministry of Education, Nanchang Hangkong University, Nanchang 330063, China

[2] Jiangxi Hongdu Aviation Industry Group Co., Ltd., Nanchang 330000, China

Corresponding author: Zhenhua Chen
Email: zhenhuachen@yeah.net

## Abstract

Aircraft horizontal-stabilizer honeycomb sandwich composite panels have complex structures, large inspection areas, and diverse defect types. Ultrasonic C-scan imaging can directly visualize the bonding condition between the face sheet and the honeycomb core; however, the large number of inspection images is conventionally interpreted by experienced inspectors, resulting in low evaluation efficiency and strong subjectivity. This study therefore proposes an intelligent classification method for ultrasonic C-scan images of the bonding interface in honeycomb sandwich composite panels. First, ultrasonic C-scan images of the face-sheet–honeycomb interface are acquired by interface-echo tracking, and a strategy is developed to expand the image dataset. Second, the images are divided into three target-region classes according to their amplitude distributions, representing three bonding-condition categories. Finally, a ResNet50 network is constructed, trained, and evaluated for bonding-condition classification. The results demonstrate that interface-echo tracking can generate C-scan images of the honeycomb bonding interface and that ResNet50 can identify the three target-region classes with good stability and accuracy.

**Keywords:** Honeycomb sandwich composite panel; Water-jet-coupled focused ultrasonic testing; Deep learning; Intelligent classification; Bonding condition; Ultrasonic C-scan image

## 1 Introduction

Honeycomb sandwich composite panels are widely used in aircraft structures because of their low density, high stiffness-to-weight and strength-to-weight ratios, and favorable impact resistance [1-3]. Their complex construction and service environments may lead to face-sheet delamination, face-sheet–core debonding, core crushing, and local buckling or wrinkling [4-6]. In particular, interface disbonding reduces structural strength and stability and may seriously compromise component safety [7,8]. Ultrasonic testing is widely used for the inspection of composite structures because it is sensitive to both surface and subsurface damage and can support one-sided inspection. Pulse-echo and through-transmission configurations are commonly employed, while C-scan imaging provides a plan-view representation of the inspected region [9]. Inspection of aircraft horizontal-stabilizer panels produces large numbers of C-scan images. Manual interpretation is inefficient, depends strongly on inspector experience, and may produce inconsistent decisions. Deep learning has therefore been applied to automatic defect classification in nondestructive testing. Hu et al. [10] reported 95.56% accuracy for phased-array crack images using an ODDC-enhanced YOLOv7-tiny model. Meng et al. [11] developed a deep-convolutional-neural-network framework for classifying ultrasonic signals from CFRP specimens containing voids and delaminations and subsequently visualized the classification results through C-scan imaging. Xia et al. [12] investigated deep-learning-based ultrasonic evaluation of adhesive-layer defects and demonstrated the potential of neural networks for bonded-structure assessment. Munir et al. [13] showed that CNNs outperformed DNNs for ultrasonic weld-flaw classification under high-noise conditions. Nevertheless, intelligent classification

of ultrasonic images from honeycomb bonding interfaces remains challenging because the periodic honeycomb patterns are highly similar and image differences between adjacent bonding conditions can be subtle.

To address these issues, this study proposes an intelligent classification framework for evaluating bonding conditions in honeycomb sandwich composite panels based on interface-echo tracking and a transfer-learning-based ResNet50 network. As illustrated in Fig. 1, the proposed framework consists of three stages: ultrasonic data acquisition, C-scan reconstruction and dataset construction, and ResNet50-based classification and evaluation. First, the adhesive-layer–honeycomb interface echo $f_3$ is located with reference to the water–face-sheet interface echo $f_1$, and its amplitude is used to reconstruct the C-scan image. Gaussian filtering and bicubic interpolation are subsequently applied to improve image quality. Sliding-window patches are then extracted and classified into three bonding conditions according to the proportion of pixels exceeding the prescribed amplitude threshold. Next, the original labeled patches are partitioned using group-wise stratified five-fold cross-validation. Data augmentation is performed only on the training data after each fold partition, whereas the corresponding validation fold remains in its original form. Hyperparameter selection is also conducted exclusively within the training folds to prevent information leakage. Finally, a transfer-learning-based ResNet50 model is fine-tuned to classify the three bonding conditions, and its performance is evaluated using accuracy, precision, recall, $F_1$-score, and confusion matrices. The engineering applicability of the proposed method is further assessed using an independent honeycomb sandwich panel..

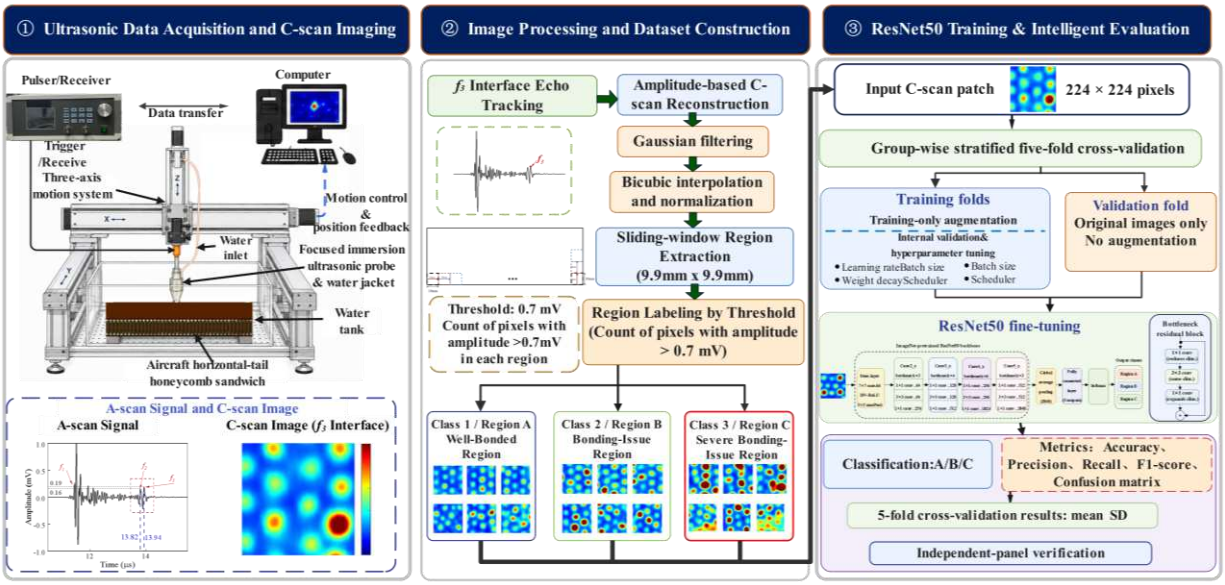



Fig. 1. Overall workflow of the proposed ultrasonic bonding-quality characterization method

## 2 Test Specimen and Experimental Methods

Reflected echoes from the honeycomb structure were acquired and imaged using water-jet-coupled focused ultrasonic testing. Compared with through-transmission testing, the pulse-echo method avoids superposition of defect indications along the thickness direction and provides more accurate information for defect localization and sizing. Its single-sided probe arrangement also offers better environmental adaptability for in-service inspection. A 65 × 180 mm region cut from an aircraft horizontal-stabilizer honeycomb sandwich composite panel was used as the specimen. The carbon-fibre-reinforced polymer face sheet was 3.7 mm thick, the aramid-paper honeycomb core was 88 mm thick with a wall thickness of 0.1 mm and a cell diameter of 3 mm, and the adhesive was an epoxy resin, as shown in Fig. 2a. C-scan imaging was performed using a 15 MHz focused probe

with a 6 mm element diameter and a 19.2 mm focal length in water. The water path was adjusted to 8.56 mm, and one A-scan was acquired at each 0.1 mm scan increment. The echoes consisted of the water–face-sheet echo $f_1$, face-sheet–adhesive echo $f_2$, and adhesive–honeycomb echo $f_3$. The arrival times of $f_2$ and $f_3$ were 13.82 and 13.94 μs, respectively; their 0.12 μs difference corresponded to the adhesive-layer thickness (Fig. 2b and c).

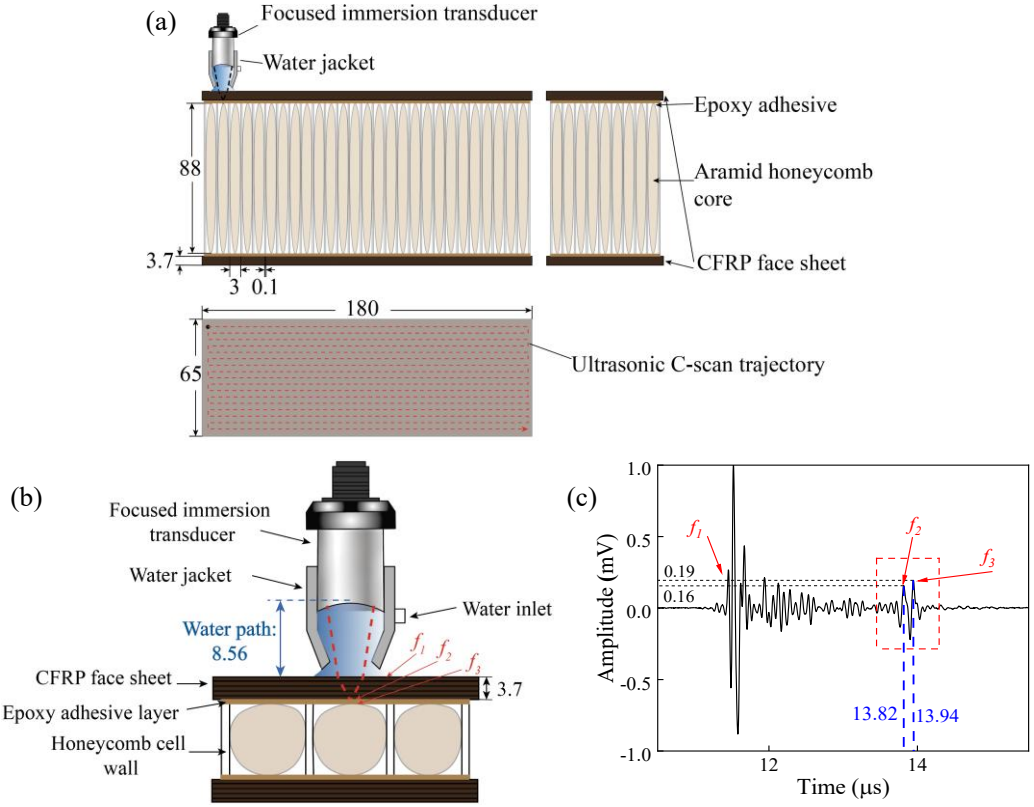



Fig. 2 Test specimen and experimental method:**a** Three-view drawing of the specimen and C-scan trajectory; **b** Schematic of water-jet-coupled focused ultrasonic testing; **c** A-scan signal

The face-sheet–adhesive interface echo $f_2$ can reflect the bonding condition of the upper face sheet but cannot characterize the adhesive layer or the adhesive–honeycomb interface. The adhesive–honeycomb interface echo $f_3$ must therefore be tracked for imaging. Because the face-sheet thickness is constant, $f_3$ can be located by delaying the water–face-sheet echo $f_1$ by the propagation time through the face sheet. Figure 3 compares C-scan images formed from $f_2$ before tracking and $f_3$ after tracking. The $f_2$-based image exhibits generally high amplitudes and does not fully reveal the overall bonding condition, whereas the $f_3$-based image has good resolution and clearly shows the regular honeycomb-cell patten.

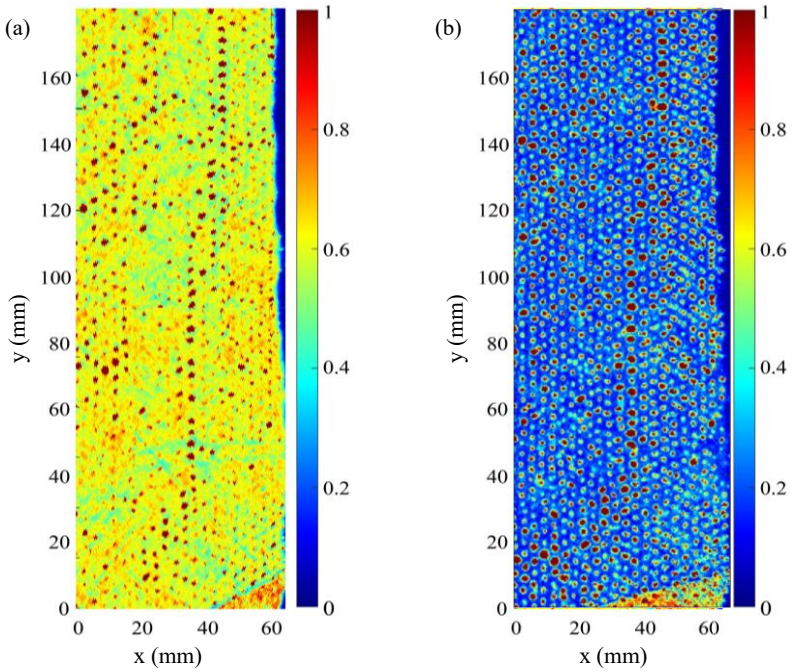



Fig. 3 Comparison of C-scan images before and after echo tracking: **a** Without echo tracking; **b** With echo tracking

Gaussian filtering is applied to reduce image noise and blurred-edge effects. The Gaussian kernel is convolved with the image, and each pixel is weighted according to its distance from the kernel centre. Pixels closer to the centre receive larger weights, so the processed amplitude is a weighted average of the original pixel and its neighbours. This operation smooths the image and suppresses noise while retaining edge information [14]. The Gaussian function is expressed as:

$$G(x,y)=\frac{1}{2\pi\sigma^2}e^{-\frac{x^2+y^2}{2\sigma^2}} \tag{1}$$

where *(x,y)* denotes the coordinates of a pixel, and $\sigma$ is the standard deviation.

After Gaussian filtering, bicubic interpolation based on 16 neighbouring pixels in a 4 × 4 neighbourhood is used to enhance spatial resolution. Cubic interpolation is first performed along the four horizontal rows, and the results are combined into four intermediate values. A second cubic interpolation is then performed vertically to obtain the new target-pixel value. This method reduces jagged edges, improves smoothness, and increases image resolution [15,16]. The bicubic interpolation is expressed as:

$$B(u,v)=\sum_{i=-1}^{2}\sum_{j=-1}^{2}a_{ij}\times W(u-i)\times W(v-j) \tag{2}$$

$$W(x)=\begin{cases}(a+2)|x|^3-(a+3)|x|^2+1, 0\le|x|<1\\ a|x|^3-5a|x|^2+8a|x|-4a, 1\le|x|<2\\ 0, |x|\ge 2\end{cases} \tag{3}$$

where *W(x)* is the interpolation weighting function; *W(u-i)* and *W(v-j)* are the horizontal and vertical weighting coefficients, respectively; *x* is the coordinate distance to the nearest pixel; a is the interpolation coefficient, normally set to −0.5; *B(u,v)* is the interpolated value at target point *(u,v)*; and $a_{ij}$ is the pixel value in the 4 × 4 neighbourhood.

After Gaussian filtering and bicubic interpolation, image noise is significantly suppressed and edges are smoothed, resulting in improved image quality, as shown in Fig. 4. In the C-scan images, the red regions correspond to high-amplitude areas, indicating unbonded defects, whereas the blue regions correspond to low-amplitude areas, indicating well-bonded regions.

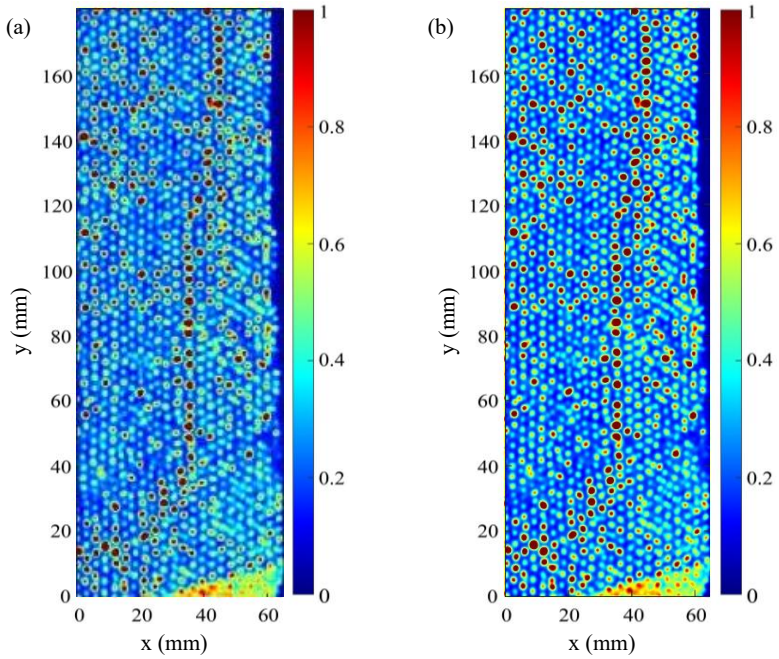



Fig. 4 Ultrasonic C-scan images after image processing: **a** After Gaussian filtering; **b** After bicubic interpolation

## 3 Inspection-Image Analysis and Dataset Augmentation

Metallographic examination was used to relate C-scan features to honeycomb bonding conditions. Figure 5 compares C-scan images and cross-sectional metallographs at two locations. In Fig. 5(a), separated circular yellow-red regions correspond to high interface-echo amplitudes from unbonded portions of the honeycomb cells. The spaces between these regions indicate well-bonded face-sheet–honeycomb areas, where the ultrasonic wave is transmitted into the core and the reflected echo is weak. The smallest high-amplitude C-scan region corresponds to the thickest adhesive layer (0.45 mm), whereas the largest high-amplitude region corresponds to the thinnest adhesive layer (0.16 mm), because a thicker adhesive layer produces greater attenuation. Figure 5(b) shows an additional high-amplitude yellow region between the circular features, indicating disbonding between the face sheet and a honeycomb wall. Thus, the amplitude distribution in the C-scan image reflects both adhesive thickness and bonding condition; high-amplitude interface echoes generally indicate poorer bonding.

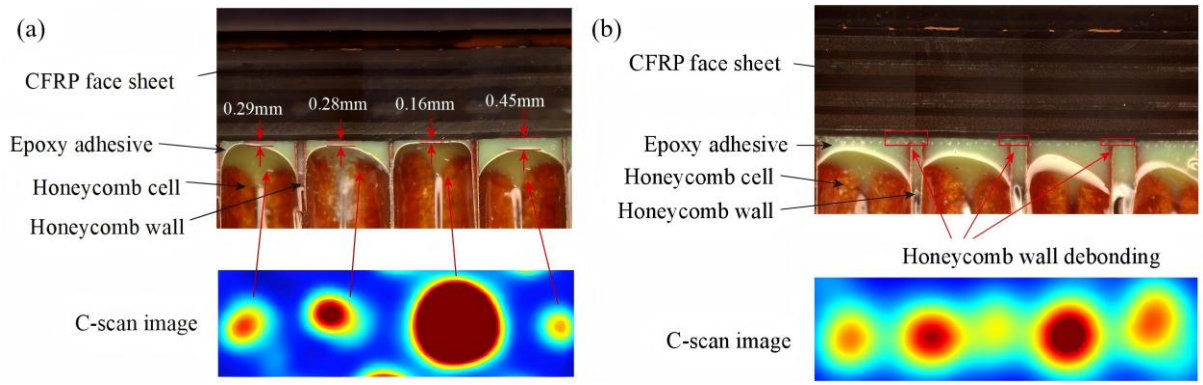



Fig. 5 Comparison of metallographic sections and ultrasonic C-scan images: **a** Metallographic specimen from a region with large cell-image variations; **b** Metallographic specimen from a disbonded region

A group of honeycomb cells within a local region collectively carries the external load and determines panel performance; evaluating a region is therefore more meaningful than evaluating a single cell. A 9.9 × 9.9 mm sliding window was used to randomly extract 300 square patches from the C-scan image. Because obtaining a sufficiently large number of experimentally verified bonding-condition labels is challenging, a threshold-based labeling strategy was adopted to construct preliminary class labels from ultrasonic amplitude distributions. These labels were subsequently used for supervised training of the ResNet50 model. Specifically, classification was based on the cumulative number of pixels in each target region whose amplitudes exceeded 0.7 mV. Taking the maximum above-threshold pixel count Nmax among all target regions as the reference, target regions A, B, and C are defined as follows:

$$\text{Target region A: } N_A \le N_{\max} \times 20\% \tag{4}$$

$$\text{Target region B: } N_{\max} \times 20\% < N_B < N_{\max} \times 40\% \tag{5}$$

$$\text{Target region C: } N_C \ge N_{\max} \times 40\% \tag{6}$$

where $N_A$, $N_B$, and $N_C$ denote the numbers of pixels with amplitudes exceeding 0.7 mV in target regions A, B, and C, respectively.

The target-region C-scan images defined by Eqs. (4)–(6) are shown in Fig. 6. Region A has the fewest above-threshold pixels and exhibits an orderly, intact honeycomb pattern, representing a well-bonded region. Region C has the most above-threshold pixels and exhibits merged, irregular honeycomb indications, representing a region with severe bonding problems. Region B lies between regions A and C and represents an intermediate bonding problem.

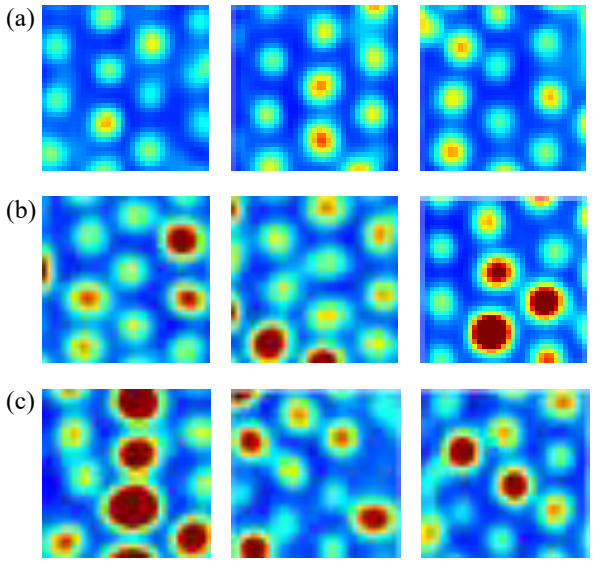



Fig. 6 Examples of the three target-region classes: **a** Target region A; **b** Target region B; **c** Target region C

Among the 300 original patches extracted using the sliding-window method, classes A, B, and C contained 99, 95, and 106 samples, respectively. Considering the limited sample size, stratified five-fold cross-validation was adopted. In each fold, one subset served as the outer validation set, while the remaining four subsets were used for training. After the five-fold partitioning, mirroring, rotation, and random-noise perturbation were applied exclusively to the training portion [17]. Representative examples of the original and augmented C-scan patches are shown in Fig. 7, including mirrored, rotated, noise-perturbed, and combined transformations. This procedure yielded approximately 2,200 training images per fold, with minor differences arising from the class composition of each fold. The outer validation images always remained in their original form and were not involved in any augmentation procedure. Across the five folds, the outer validation subsets collectively covered all 300 original patches; therefore, no additional fixed test set was constructed.

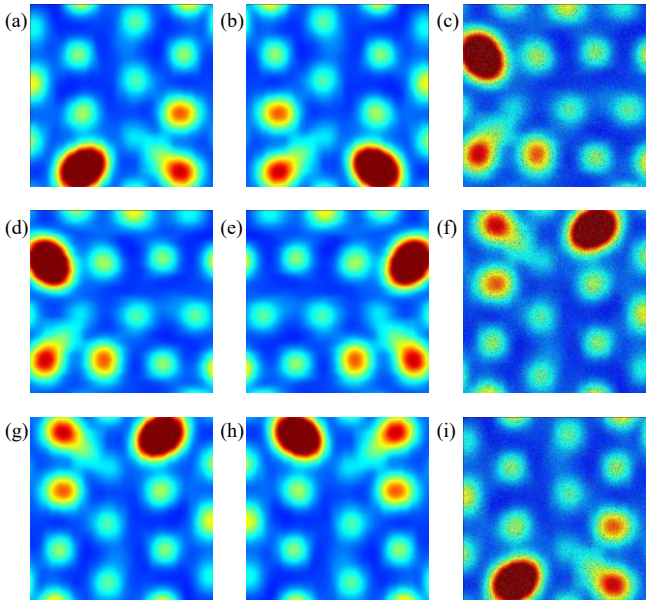



Fig. 7 Examples of training-image augmentation: **a** Original image; **b** Mirrored image; **c** Noise perturbation; **d** 90° rotation; **e** 90° rotation + mirroring; **f** 90° rotation + noise; **g** 180° rotation; **h** 180° rotation + mirroring; **i** 180° rotation + noise

## 4 Deep-Learning Network and Performance Metrics

ResNet50, originally proposed by He et al. [18], mainly comprises convolutional layers, global average pooling, and a fully connected layer. As shown in Fig. 8(a), its architecture can be divided into seven stages. Stage 1

contains a 7 × 7 convolution, batch normalization (BN), ReLU activation, and max pooling for shallow-feature extraction. Stages 2–5 correspond to four residual modules (Conv2_x–Conv5_x) containing 3, 4, 6, and 3 bottleneck blocks, respectively. Each bottleneck block contains 1 × 1, 3 × 3, and 1 × 1 convolutions: the first reduces dimensionality, the second extracts features, and the third restores dimensionality and expands the channels. Stage 6 uses global average pooling (GAP) to compress each two-dimensional feature map into a one-dimensional vector while retaining global semantic information. In Stage 7, a fully connected layer and Softmax function output the probabilities of the three bonding-condition classes.

The core of ResNet50 is the residual block. A shortcut connection passes the input directly to the output so that the network learns a residual mapping $F(x)$, with $H(x) = F(x) + x$. When $F(x) = 0$, the residual block approximates an identity mapping. The identity shortcut provides a direct path for forward information and backward gradient propagation, thereby facilitating the optimization of deep networks and alleviating the network-degradation problem [18,19]. Subsequent studies have further demonstrated that network depth and residual-block design strongly influence the training efficiency and generalization performance of residual networks [20,21]. By stacking multiple residual blocks, ResNet50 is capable of extracting discriminative features from ultrasonic C-scan images and distinguish subtle differences among the three bonding conditions.

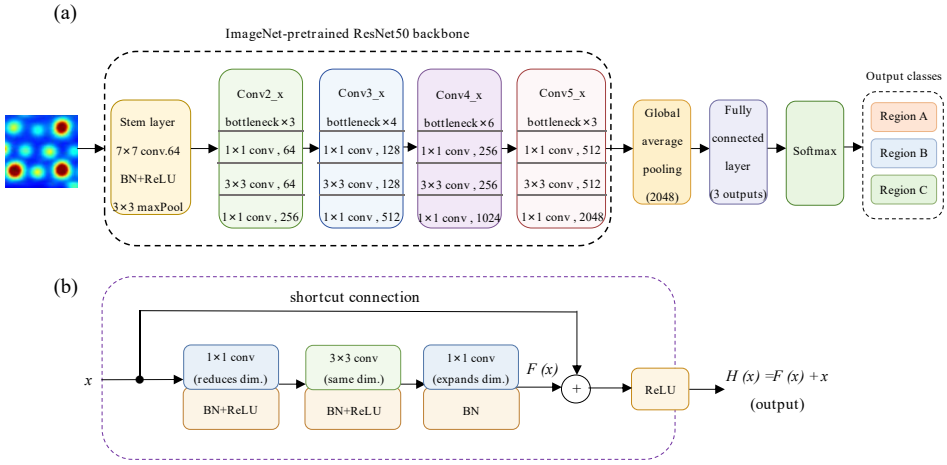



Fig. 8 ResNet50 network: **a** Network architecture; **b** Residual-block architecture

Classification performance was evaluated using accuracy, precision, recall, and the $F_1$ score [22] Accuracy was calculated over all samples, whereas precision, recall, and the $F_1$ score were calculated separately for each class as follows:

$$Accuracy = \frac{\sum_{i=1}^{K} TP_i}{N} \tag{7}$$

$$\mathrm{Pr}ecision_i = \frac{TP_i}{TP_i + FP_i} \tag{8}$$

$$\mathrm{Re}call_i = \frac{TP_i}{TP_i + FN_i} \tag{9}$$

$$F_{1,i} = \frac{2TP_i}{2TP_i + FP_i + FN_i} \tag{10}$$

where $TP_i$, $FP_i$, and $FN_i$ are the true-positive, false-positive, and false-negative counts for class $i$, respectively; $N$ is the total number of samples. Accuracy measures overall classification performance, while precision, recall, and $F_1$ characterize class-wise performance.

Macro precision, macro recall, and macro $F_1$ are obtained by averaging the corresponding class-wise metrics over the three target-region classes.

## 5 Network Training and Performance Testing

### 5.1 ResNet50 Training and Classification Performance

The ResNet50 network was trained and evaluated using the constructed ultrasonic C-scan image dataset. Considering the limited sample size, the 300 original images were stratified by class into five mutually exclusive folds. In each of the five rounds, one fold was used for validation and the remaining four folds were used for training. To prevent data leakage, random rotation, mirroring, and random-noise perturbation were applied exclusively to the training images after fold partitioning, while the validation images remained unaugmented.

Within the training portion of each fold, an internal validation split was used for hyperparameter selection without involving the held-out validation fold. The hyperparameter space comprised 120 possible combinations of learning rate (0.0001–0.0010 in increments of 0.0001), batch size (8, 12, or 16), weight decay (0 or 0.0001), and learning-rate scheduling (disabled or enabled). Considering the computational cost, up to 24 candidate configurations were evaluated per fold, with each configuration trained for 12 tuning epochs. The optimal configuration was subsequently used for formal training with the cross-entropy loss function and the stochastic gradient descent (SGD) optimizer for 150 epochs, with the momentum set to 0.9. Training and validation performance was recorded at each epoch, and the checkpoint with the highest validation accuracy was retained for each fold.

As shown in Fig. 9, the training accuracy increased rapidly during the initial epochs and gradually converged, while the validation accuracy increased markedly at the beginning and subsequently fluctuated within a stable range. These trends demonstrate that the ResNet50 model effectively learned discriminative bonding-condition features from the ultrasonic C-scan images and exhibited good convergence and training stability.

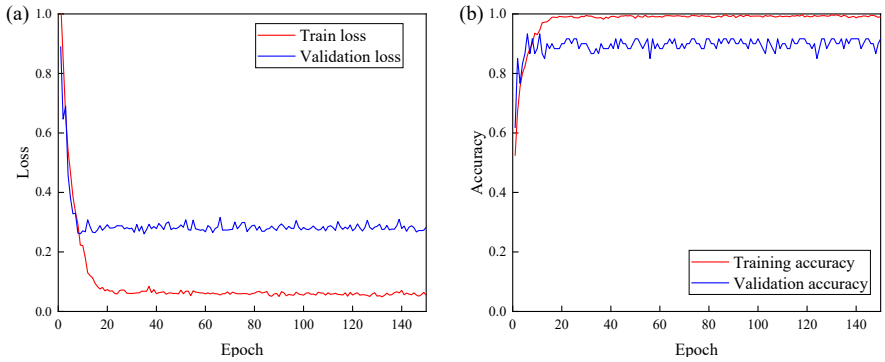



Fig. 9 Training curves of the ResNet50 model during five-fold cross-validation

The fold-wise classification accuracies were 90.16%, 93.33%, 85.00%, 90.00%, and 91.53%, yielding a mean accuracy of 90.00% ± 3.10%. The reported performance represents the estimated generalization capability obtained from five-fold cross-validation rather than the performance evaluated on an additional independent test set. The corresponding macro precision, macro recall, and macro F1-score were 90.51% ± 3.46%, 89.96% ±

3.20%, and 89.95% ± 3.19%, respectively, indicating stable classification performance across different data partitions.

Predictions from the five validation folds were combined to construct the out-of-fold confusion matrix shown in Fig. 10. The resulting accuracy was 90.00%, with macro precision, macro recall, and macro $F_1$-score values of 90.06%, 89.96%, and 89.99%, respectively. For regions A, B, and C, the precision/recall/$F_1$-score values were 96.88%/93.94%/95.38%, 82.83%/86.32%/84.54%, and 90.48%/89.62%/90.05%, respectively. Most errors occurred between the adjacent B and C classes: 10 B samples were misclassified as C, and 11 C samples were misclassified as B. No direct confusion occurred between regions A and C, consistent with the similarity of ultrasonic features in transitional bonding regions.

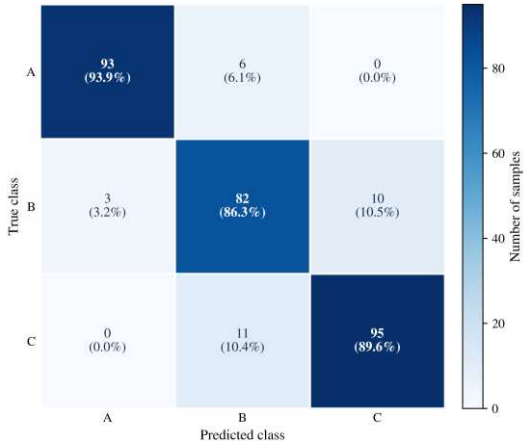



Fig. 10 Aggregated out-of-fold confusion matrix

## 5.2 Intelligent Recognition Capability Test

A separate 40 × 300 mm honeycomb sandwich composite panel was inspected, and an ultrasonic C-scan image was acquired. A 9.9 × 9.9 mm sliding window with a stride of 9.9 mm was used to extract 120 image patches while retaining their spatial coordinates, as shown in Fig. 11a. The patches were classified using both the mathematical threshold method and the deep-learning model and were color-coded as follows: green for region A, yellow for region B, and red for region C. The network also returned a confidence score for each prediction. Predictions with confidence below 0.6 were rejected as uncertain and displayed in white, indicating regions requiring further expert assessment. The mathematical classification map and the reconstructed deep-learning classification maps shown in Fig. 11b – d exhibit good overall agreement.

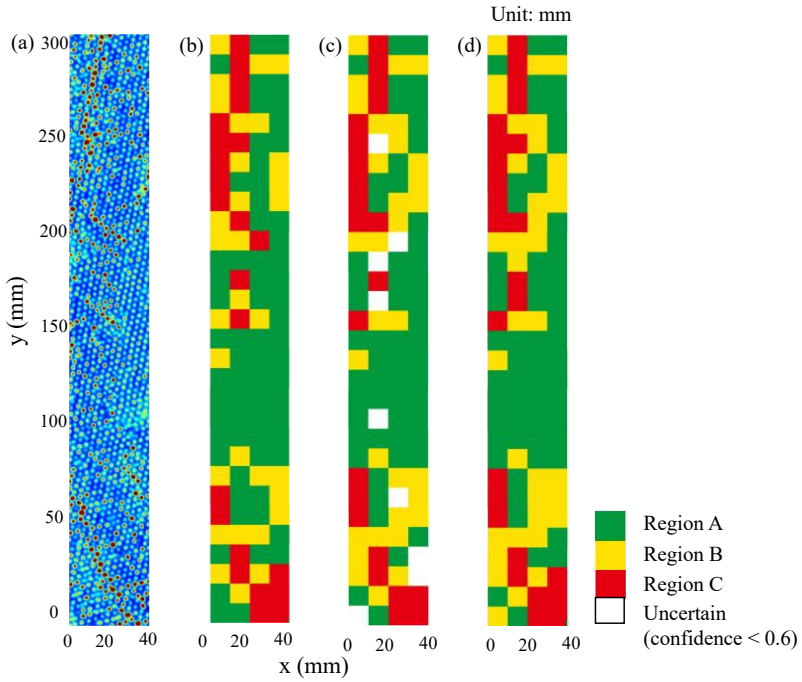



Fig. 11 Bonding-condition classification and spatial reconstruction for the separate panel: **a** ultrasonic C-scan image; **b** mathematical-threshold classification map; **c** ResNet50 classification map with confidence-based rejection (threshold = 0.6); **d** ResNet50 classification map without confidence-based rejection

Using the mathematical partition as the reference labels, the class-wise recall of the ResNet50 model for regions A, B, and C was 87.9%, 83.9%, and 91.3%, respectively, as calculated using Eq. (9). When predictions with confidence below 0.6 were rejected as uncertain, 111 of the 120 patches were retained, corresponding to a coverage of 92.5%. For the retained predictions, the selective class-wise recall for regions A, B, and C increased to 91.8%, 86.7%, and 95.0%, respectively (Fig. 12a). These increases should be interpreted as improved conditional performance on the retained predictions rather than as an improvement over all 120 patches, because confidence-based rejection introduces a trade-off between classification performance and sample coverage.

Without confidence-based rejection, the dominant misclassification types were A→B (6.7%) and B→C (3.3%). After confidence-based rejection, these rates decreased to 4.5% and 2.7%, respectively, while the rate of each remaining misclassification type was no greater than 1.7% (Fig. 12b). No direct misclassification occurred between regions A and C. Because the dominant errors were A→B and B→C, most misclassifications overestimated the severity of the bonding condition, which is consistent with the conservative evaluation philosophy of nondestructive testing.

It should be noted that the reference labels were generated using a hard-threshold mathematical method. Therefore, this engineering test primarily evaluates the agreement between the ResNet50 predictions and the mathematical partition rather than validating the actual bonding condition directly. In future engineering applications, a larger number of naturally occurring samples should be calibrated through combined nondestructive inspection and destructive validation. Such calibration would allow the hard boundaries defined by mathematical thresholds to be replaced with data-driven soft boundaries, thereby improving the model's generalization and bonding-condition recognition capabilities.

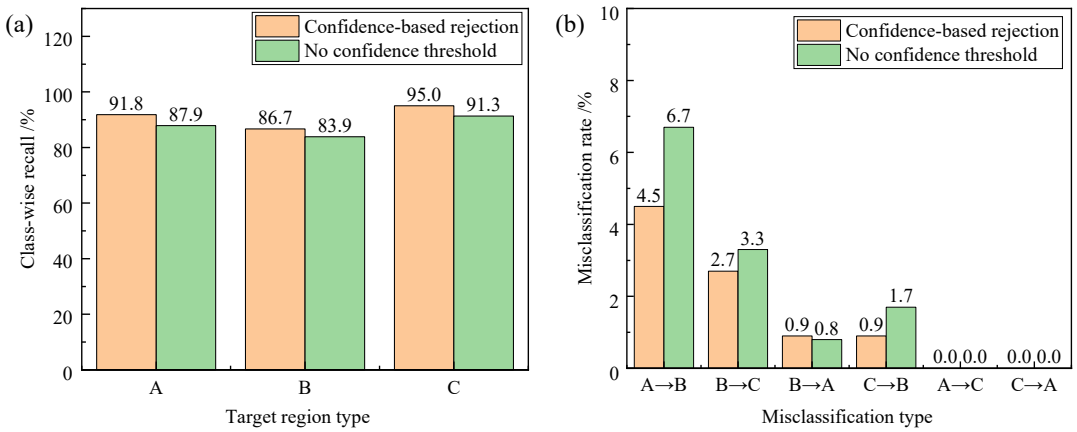



Fig. 12 Class-wise recall and misclassification analysis for the separate-panel test: **a** Class-wise recall; **b** Distribution of misclassification types

## 6 Conclusions

1) Tracking and imaging the adhesive–honeycomb interface echo provides an effective indication of the bonding condition between the face sheet and the honeycomb core. Gaussian filtering and bicubic interpolation effectively suppress noise and improve spatial resolution.

2) A sliding-window method was developed to extract patches from ultrasonic C-scan images. In combination with mathematical classification and training-only augmentation, it efficiently constructed a database suitable for deep-learning training from a 65 × 180 mm C-scan image.

3) In the independent-panel test, confidence-based rejection retained 111 of the 120 patches, corresponding to a coverage of 92.5%, and yielded selective class-wise recalls of 91.8%, 86.7%, and 95.0% for regions A, B, and C, respectively.

4) After confidence screening, most misclassifications overestimated the severity of the bonding condition, reflecting a conservative evaluation criterion consistent with the safety-oriented requirements of nondestructive testing and providing target regions for further expert confirmation.

## Declarations

***Funding***

The Article Processing Charge (APC) for the publication of this research was funded by the National Natural Science Foundation of China (Grant No. 12464059) and the Jiangxi Provincial National Science and Technology Award Reserve Project Cultivation (Grant No. 20223AEI91009).

***Competing interests***

The authors have no relevant financial or non-financial interests to disclose.

***Ethics approval***

Not applicable. This study did not involve human participants or animals.

***Consent to participate***

Not applicable.

***Consent for publication***

Not applicable.

***Data availability***

The datasets generated and analyzed during the current study are available from the corresponding author on reasonable request.

***Code availability***

The code used for image processing, model training, and performance evaluation in this study is available from the corresponding author on reasonable request.

***Authors' contributions***

Yating Ni: Formal analysis, Software, Visualization, Validation. Zhenhua Chen: Conceptualization, Methodology. Simin Tu: Data curation, Visualization. Junyan Zhang: Resources, Validation. Liu Yang: Validation. Chao Lu: Supervision, Project administration. All authors reviewed the manuscript draft and revised it critically on intellectual content. All authors approved the final version of the manuscript to be published.

## References


1. Krzyżak, A., Mazur, M., Gajewski, M., Drozd, K., Komorek, A., Przybyłek, P.: Sandwich structured composites for aeronautics: methods of manufacturing affecting some mechanical properties. International Journal of Aerospace Engineering. **2016**, 7816912 (2016). https://doi.org/10.1155/2016/7816912
2. Wang, W., Li, F., Ren, F., Wei, X., Xiong, J.: Research progress on structural design methods and mechanical properties of lightweight high-strength composite lattice stiffened shell structure. Acta Aeronautica et Astronautica Sinica. **45**, 530001 (2024). https://doi.org/10.7527/S1000-6893.2024.30001
3. Towsyfyan, H., Biguri, A., Boardman, R., Blumensath, T.: Successes and challenges in non-destructive testing of aircraft composite structures. Chinese Journal of Aeronautics. **33**, 771-791 (2020). https://doi.org/10.1016/j.cja.2019.09.017
4. Yan, B., Wang, X., Pan, S., Tong, M., Yu, J., Liu, F.: Stability and failure of the edge-closed honeycomb sandwich panels with face/core debonding. Applied Sciences. **10**, 7457 (2020). https://doi.org/10.3390/app10217457
5. Chen, H.Q., Xu, Z.Y., Qu, Z.Y., et al.: Review of nondestructive testing methods for honeycomb sandwich structures. Mater. Rep. **38**(10), 296–310 (2024) (in Chinese). https://doi.org/10.11896/cldb.22090208
6. Nsengiyumva, W., Zhong, S., Lin, J., Zhang, Q., Zhong, J., Huang, Y.: Advances, limitations and prospects of nondestructive testing and evaluation of thick composites and sandwich structures: A state-of-the-art review. Composite Structures. **256**, 112951 (2021). https://doi.org/10.1016/j.compstruct.2020.112951
7. Yu, Z., Guo, Y., Sun, H., Zhang, J., Sun, X.: Recent progress in structural integrity of novel materials and advanced techniques. Acta Aeronautica et Astronautica Sinica. **45**, 029888 (2024). https://doi.org/10.7527/S1000-6893.2024.29888
8. Tan, Z., Wang, M.Q., Liu, K.C., et al.: Research on AirCoupling Ultrasonic Testing Technology for Debonding of Honeycomb Sandwich Structure. Piezoelectr. Acoustoopt. **43**(6), 799–804 (2021) (in Chinese). https://doi.org/10.11977/j.issn.1004-2474.2021.06.016
9. Senthilkumar, M., Sreekanth, T. G., Manikanta Reddy, S.: Nondestructive health monitoring techniques for composite materials: A review. Polymers and Polymer Composites. **29**, 528-540 (2021). https://doi.org/10.1177/0967391120921701

10. Hu, F., Gou, H. Y., Yang, H. Z., Yan, H., Ni, Y. Q., Wang, Y. W.: Automatic PAUT crack detection and depth identification framework based on inspection robot and deep learning method. Journal of Infrastructure Intelligence and Resilience. **4**, 100113 (2025). https://doi.org/10.1016/j.iintel.2024.100113
11. Meng, M., Chua, Y. J., Wouterson, E., Ong, C. P. K.: Ultrasonic signal classification and imaging system for composite materials via deep convolutional neural networks. Neurocomputing. **257**, 128-135 (2017). https://doi.org/10.1016/j.neucom.2016.11.066
12. Xia, G.R., Wei, D.T., Liu, Z.J., et al.: Damage identification of the adhesive layer in bonded-steel members based on deep learning. J. Exp. Mech. **39**(4), 399–412 (2024) (in Chinese). https://doi.org/10.7520/1001-4888-23-268
13. Munir, N., Kim, H. J., Park, J., Song, S. J., Kang, S. S.: Convolutional neural network for ultrasonic weldment flaw classification in noisy conditions. Ultrasonic. **94**, 74-81 (2019). https://doi.org/10.1016/j.ultras.2018.12.001
14. Young, I. T., Van Vliet, L. J.: Recursive implementation of the Gaussian filter. Signal Processing. **44**, 139-151 (1995). https://doi.org/10.1016/0165-1684(95)00020-E
15. Keys, R.: Cubic convolution interpolation for digital image processing. IEEE Transactions on Acoustics, Speech, and Signal Processing. **29**, 1153-1160 (1981). https://doi.org/10.1109/TASSP.1981.1163711
16. Meijering E.: A chronology of interpolation: From ancient astronomy to modern signal and image processing. Proceedings of the IEEE. **90**(3), 319–342 (2002). https://doi.org/10.1109/5.993400
17. Shorten, C., Khoshgoftaar, T. M.: A survey on image data augmentation for deep learning. Journal of Big Data. **6**, 60 (2019). https://doi.org/10.1186/s40537-019-0197-0
18. He, K., Zhang, X., Ren, S., Sun, J.: Deep residual learning for image recognition. In: Proceedings of the IEEE Conference on Computer Vision and Pattern Recognition (CVPR), Las Vegas, NV, USA, pp. 770–778 (2016). https://doi.org/10.1109/CVPR.2016.90
19. He, K., Zhang, X., Ren, S., Sun, J.: Identity mappings in deep residual networks. In: Proc. European Conference on Computer Vision (Cham, 2016), pp. 630–645. https://doi.org/10.1007/978-3-319-46493-0_38
20. Huang, G., Sun, Y., Liu, Z., Sedra, D., Weinberger, K.Q.: Deep networks with stochastic depth. In: Proc. European Conference on Computer Vision (Cham, 2016), pp. 646–661. https://doi.org/10.1007/978-3-319-46493-0_39
21. Zagoruyko, S., Komodakis, N.: Wide residual networks. arXiv:1605.07146 (2016). https://doi.org/10.48550/arXiv.1605.07146
22. Sokolova, M., Lapalme, G.: A systematic analysis of performance measures for classification tasks. Information Processing & Management. **45**, 427–437 (2009). https://doi.org/10.1016/j.ipm.2009.03.002